Article

Physico-Chemical Properties and In Vitro Antifungal Evaluation of Samarium Doped Hydroxyapatite Coatings

Steluta Carmen Ciobanu [1]**, Simona Liliana Iconaru** [1] **, Daniela Predoi** [1]**,**
Alina Mihaela Prodan [2,3] **and Mihai Valentin Predoi** [4,*]

[1] National Institute of Materials Physics, Atomistilor Street, No. 405A, P.O. Box MG 07, 077125 Magurele, Romania; carmen.ciobanu@infim.ro or ciobanucs@gmail.com (S.C.C.); simona.iconaru@infim.ro or simonaiconaru@gmail.com (S.L.I.); dpredoi@infim.ro or dpredoi@gmail.com (D.P.)

[2] Department of General Surgery, Carol Davila University of Medicine and Pharmacy, 8 Eroii Sanitari, Sector 5, 050474 Bucharest, Romania; prodan1084@gmail.com

[3] Emergency Hospital Floreasca Bucharest, 8 Calea Floreasca, 014461 Bucharest, Romania

[4] Department of Mechanics, University Politehnica of Bucharest, BN 002, 313 Splaiul Independentei, Sector 6, 060042 Bucharest, Romania

[*] Correspondence: mihai.predoi@upb.ro or predoi@gmail.com

check for
updates

Abstract: Hydroxyapatite (HAp) and samarium doped hydroxyapatite, $Ca_{10-x}Sm_x(PO_4)_6(OH)_2$, $x_{Sm} = 0.05$, (5SmHAp), coatings were prepared by sol-gel process using the dip coating method. The stability of 5SmHAp suspension was evaluated by ultrasound measurements. Fourier transform infrared spectroscopy (FTIR) was used to examine the optical characteristics of HAp and 5SmHAp nanoparticles in suspension and coatings. The FTIR analysis revealed the presence of the functional groups specific to the structure of hydroxyapatite in the 5SmHAp suspensions and coatings. The morphology of 5SmHAp nanoparticles in suspension was evaluated by transmission electron microscopy (TEM). Moreover, scanning electron microscope (SEM) was used to evaluate the morphology of nanoparticle in suspension and the morphology of the surface on the coating. The SEM and TEM studies on 5SmHAp nanoparticles in suspension showed that our samples consist of nanometric particles with elongated morphology. The SEM micrographs of HAp and 5SmHAp coatings pointed out that the coatings are continuous and homogeneous. The surface morphology of the 5SmHAp coatings was also assessed by Atomic Force Microscopy (AFM) studies. The AFM results emphasized that the coatings presented the morphology of a uniformly deposited layer with no cracks and fissures. The crystal structure of 5SmHAp coating was characterized by X-ray diffraction (XRD). The surface composition of 5SmHAp coating was analyzed by X-ray photoelectron spectroscopy (XPS). The XRD and XPS analysis shown that the Sm^{3+} ions have been incorporated into the 5SmHAp synthesized material. The antifungal properties of the 5SmHAp suspensions and coatings were studied using *Candida albicans* ATCC 10231 (*C. albicans*) fungal strains. The quantitative results of the antifungal assay showed that colony forming unity development was inhibited from the early phase of adherence in the case of both suspensions and coatings. Furthermore, the adhesion, cell proliferation and biofilm formation of the *C. albicans* were also investigated by AFM, SEM and Confocal Laser Scanning Microscopy (CLSM) techniques. The results highlighted that the *C. albicans* adhesion and cell development was inhibited by the 5SmHAp coatings. Moreover, the data also revealed that the 5SmHAp coatings were effective in stopping the biofilm formation on their surface. The toxicity of the 5SmHap was also investigated in vitro using HeLa cell line.

Keywords: samarium; hydroxyapatite; dip coating method; antifungal activity

1. Introduction

Currently, the use of nanoparticles and coatings in the medical field is on an upward trend due to their remarkable properties that make them effective in many ways, starting from the fight against pathogenic microorganisms and ending with their antitumoral activity [1]. One of the most used biomaterials in the biomedical field is hydroxyapatite (HAp, $Ca_{10}(PO_4)_6(OH)_2$) which is the main mineral component of bone tissue. Hydroxyapatite, due to his unique biological properties, such as biocompatibility, low citotoxity, osteoconductivity, bioactivity and so forth [2–4], is used in various applications in the medical field like implantology (metal prosthesis coating material, etc.) [5], dentistry [5], drug and gene delivery systems [6,7], as an antimicrobial agent [8], in bioimaging [9] and so forth.

In addition, due to its hexagonal structure, HAp on the one hand has the capacity to incorporate in its structure various ions (Eu^{3+}, Ag^+, Mg^{2+}, Zn^{2+}, and Sm^{3+}, etc.) [10–12] and on the other hand the HAp surface can be modified with various biopolymers/drugs [13], which leads to an improvement of the biological and physico-chemical properties, thus making HAp more efficient and useful for the medical sphere [2]. Hydroxyapatite can be obtained in various forms, from powder/gel and reaching to thin layers/coatings by various synthesis methods, among which we mention the sol-gel method, coprecipitation (these are often used to obtain powders/gels), dip coating, spin coating, magnetron sputering and so forth (the latter being used to obtain thin HAp coatings) [14]. These methods, by controlling the synthesis parameters, allow the obtaining of both powders with nanometric/micrometric dimensions and the desired morphology and uniform and homogeneous layers [14].

In the current context of increasing the resistance of microorganisms to antibiotic treatment, recent studies have shown that doping hydroxyapatite with antimicrobial ions and the use of these new materials may be a viable alternative to conventional antibiotic treatment after implant surgery [2,5,10]. Recent studies reported in the literature have shown that the dopping of hydroxyapatite with lanthanide ions, especialy Samarium (Sm^{3+}), leads to enhanced biological and antimicrobial properties [5,10,15,16]. According to these studies, Sm^{3+} doped HAp exihibits great antibacterial activity against bacterial strain such as *Staphylococcus aureus* (ATCC 25923), *Escherichia coli* (ATCC 25922), *Staphylococcus epidermidis* (ATCC 35984/RP62A), *Enterococcus faecalis* (ATCC 29212) and *Pseudomonas aeruginosa.*

Recently, it has been observed that the interest of researchers in the use of lanthanides in biomedical applications is increasing. Therefore, in their studies, Nakayama, et al. [17] showed that the smarium doped TiO_2 nanoparticles could improve the radiosensitising effects and could be used as theranostic agents in radiation therapy. In addition, Zhang et al. [18] showed that mesoporous bioactive glass microspheres doped with small amounts of samarium of could be used as a delivery system for doxorubicin in the treatment of bone cancer.

Also, in their recent work, Kannan et al. [19] highlighted that the presence of a samarium oxide coating on a Mg implant could prevent on the one hand the recurrence of bone tumors and metastases and on the other hand the appearance of post-implant infections.

The aim of the present research was to obtain a homogenous coating with antimicrobial properties by sol-gel process using the dip coating method on Si substrate. The evaluation of the stability of nanoparticles in suspension was conducted by ultrasound measurements. To the best of our knowledge, the samarium doped hydroxyapatite coatings with antimicrobial properties realized using the dip coating method was very little studied. The antimicrobial properties investigations of the 5SmHAp coating presented in this study revealed a very good behavior of these coatings.

2. Materials and Methods

2.1. Materials

The synthesis of hydroxyapatite and samarium doped hydroxyapatite (x_{Sm} = 0.05), $Ca_{10-x}Sm_x(PO_4)_6(OH)_2$ was effectuated using calcium nitrate tetrahydrate, $Ca(NO_3)_2 \cdot 4H_2O$ (≥99.0%), samarium nitrate hexahydrate, $Sm(NO_3)_3 \cdot 6H_2O$ (99.97% purity), ammonium hydrogen phosphate,

$(NH_4)_2HPO_4$ ($\geq$99.0%), ethanol absolute, C_2H_5OH ($\geq$99.8%) and double distilled water. The reagents, such as $Ca(NO_3)_2 \cdot 4H_2O$, $(NH_4)_2HPO_4$ and C_2H_5OH, were processed by Sigma Aldrich, St. Louis, MO, USA while $Sm(NO_3)_3 \cdot 6H_2O$ was processed by Alpha Aesar, Kandel, Germany.

2.2. Hydroxyapatite (HAp) and Samarium Doped Hydroxyapatite (SmHAp)

Samarium doped hydroxyapatite nanoparticles with the chemical formula $Ca_{10-x}Sm_x(PO_4)_6(OH)_2$, $x_{Sm} = 0.05$ were synthesized by the adapted chemical method [20] with (Ca + Sm)/P fixed to 1.67 [21–23]. The $Ca(NO_3)_2 \cdot 4H_2O$ was dissolved in 100 mL C_2H_5OH and $(NH_4)HPO_4$ was dissolved in 25 mL deionized water (DI) were mixed in a 500 mL beaker and stirred together for 1 h at room temperature. $Sm(NO_3)_3 \cdot 6H_2O$ was dissolved in 25 mL of DI water at room temperature and added drop by drop into the mixture under continuous stirring at a temperature of 100 °C. The resulting solution was stirred continuously for another 2 h at 100 °C. After that, the resulting solution was centrifuged, redispersed in ethanol absolute and stirred at 100 °C for 24 h. The hydroxyapatite nanoparticles were obtained as previously described by Ciobanu et al. [24]. The final suspension was analyzed and used to prepare the coatings.

2.3. Preparation of HAp and 5SmHAp Coatings

The HAp and 5SmHAp coatings have been deposited on the Si wafer by the sol-gel process using the dip coating method in agreement with previous studies [25]. The Si substrate was washed with ethanol absolute before coating. The 5SmHAp layer was dried at 100 °C for 4 h and heat treated at 500 °C for 2 h. Cooling was done at a rate of 5 °C/min.

2.4. Characterization Methods

Ultrasonic measurements were performed on 100 mL of concentrated suspension of 5SmHAp [22,26]. The digitalized ultrasonic signals were recorded on the digital oscilloscope (General-Electric, Krautkramer, Germany) at a very precise interval of 5.00 s. In order to have an accurate evaluation of the stability of the 5SmHAp suspension, the double distilled water (the most stable suspension) was chosen as the reference fluid, under the same experimental conditions.

The morphology of the 5SmHAp suspensions was analyzed using transmission electron microscopy (TEM) with a CM 20 (Philips-FEI, Hillsboro, OR, USA) transmission electron microscope having a Lab6 filament (Agar Scientific Ltd., Stansted, UK), which operates at 200 kV. The particle size distributions from the TEM micrographs was performed by measuring approximately 700 particles from different regions of the sample.

The morphology of 5SmHAp suspensions and coatings were evaluated by scanning electron microscopy (SEM) using a HITACHI S4500 microscope (Hitachi, Ltd., Tokyo, Japan). The 5SmHAp suspensions were prepared on a conductive carbon tape with double adhesion, dried and introduced in the microscope. The microscope was equipped with energy-dispersive X-ray spectroscopy (EDX) (Ametek EDAX Inc., Mahwah, NJ, USA) attachment operating at 20 kV. The particle size distributions from the SEM micrographs was performed by measuring approximately 200 particles from different regions of the sample. The surface morphology of the coatings was analyzed using atomic force microscopy (AFM), in a non-contact mode. The measurements were performed using a NT-MDT NTEGRA Probe NanoLaboratory system (NT-MDT, Moscow, Russia). The data was recorded with a silicon NT-MDT NSG01 cantilever coated with a 35 nm gold layer having a tetrahedral tip. The AFM micrographs were acquired on surface areas of 3×3 μm^2. The data analysis of the 2D surface topographies as well as the 3D representation of the AFM images were performed with the aid of Gwyddion 2.55 software [27].

The 5SmHAp coating was examined by the X-ray diffraction (XRD) (Bruker D8 Advance diffractometer, Billerica, MA, USA) with nickel filtered Cu Kα (Å) radiation.

The functional groups present in the prepared gel and coating were identified by Fourier-transform infrared spectroscopy (FTIR) analysis using a SpectrumBX spectrometer in the case of the prepared gel

and by Fourier-transform infrared spectroscopy -Attenuated total reflection (FTIR-ATR) spectroscopy using a Perkin Elmer SP-100 spectrometer (Waltham, MS, USA), for the coatings. The spectra were taken in the spectral range of 400 to 4000 cm^{-1} with a resolution of 4 cm^{-1}. The curve fitting analysis of the spectra was achieved using a nonlinear least-squares data-fitting algorithm [28].

X-ray Photoelectron Spectroscopy (XPS) analysis was performed using a VG ESCA 3 MK II XPS installation ($E_{k\alpha} = 1486.7$ eV). The vacuum analysis chamber pressure was $P \sim 3 \times 10^{-8}$ torr. The XPS register spectrum involved an energy window $w = 20$ eV with the resolution $R = 50$ eV and 256 recording channels. The XPS spectra were analyzed using Spectral Data Processor v 2.3 (SDP) software.

2.5. In Vitro Antifungal Activity

The effects of the 5SmHAp coatings against fungi cells were assessed using the reference fungal strain *Candida albicans* ATCC 10231 acquired from the American Type Culture Collection (ATCC, Manassas, VA, USA). The in vitro antifungal assays were performed with fungal suspensions of approximately 10^5–10^6 colony forming units (CFU)/mL obtained from 15 to 18 h bacterial cultures as previously reported [29]. The qualitative assay of the fungal biofilm development, after incubation at 24, 48, and 72 h, was assessed by the visualization of the adherent fungal cells on the substrates using atomic force microscopy (AFM), scanning electron microscopy (SEM) and confocal laser scanning microscopy (CLSM). For the AFM and SEM observation, the 5SmHAp coatings were removed from the *C. albicans* ATCC 10231 culture medium after 24, 48, and 72 h of incubation, then washed with sterile saline solution and fixed using cold methanol. For the CLSM visualization, the 5SmHAp coatings after 24, 48, and 72 h of incubations with *C. albicans* fungal culture, were washed with sterile saline buffer solution (PBS) to remove the unattached fungal cells. After that, the unattached cells were fixed with cold methanol and stained in the dark with propidium iodide (PI) for 10 min at room temperature. After the PI staining, the excess of label marker was removed using filter paper. The samples were visualized directly after staining. The CLSM studies were performed both in reflection and fluorescence modes using a Leica TCS-SP confocal microscope (Leica Camera AG, Wetzlar, Germany), equipped with a PL FLUOTAR (40_ NA 0.7) objective and an Ar ion laser with a laser line at 488 nm.

The quantitative assays of the antifungal activity of both 5SmHAp suspensions and coatings were done using an adapted method (E2149-10; ASTM International) [30,31], as previously described [32]. The experiments were performed in triplicate and the results of the results were expressed as mean ± SD. Moreover, the 3D representation of the SEM and CLSM images were obtained Image J software (ImageJ 1.51j8, National Institutes of Health, Bethesda, MD, USA) was used [33].

2.6. In Vitro Cytotoxic Assay

The toxicity of the HAp and 5SmHAp solutions and coatings was assessed using the HeLa cell line (Sigma-Aldrich Corp., St. Louis, MO, USA). The in vitro interaction of the HeLa cells with the samples was studied at three different time intervals (24, 48, and 72 h) using the methodology previously described in Predoi et al. [34]. A cell viability using live/dead cell double staining kit (purchased from Merck/Sigma-Aldrich) was also performed. The kit allowed the simultaneously staining of both viable and dead cells. The number of live and dead cells were numbered and represented as function of percentage from the number of total cells. The experiments were performed in triplicate and the data represented as mean ± SD.

3. Results

The quality of the obtained coatings by sol-gel process is influenced by many factors. The most significant element is the stability of the concentrated suspension from which the coatings are obtained. A more accurate way of evaluating the stability of the suspensions is represented by ultrasound measurements. This analysis allows evaluation of the stability of the concentrated solution as opposed to the other traditional methods in which the suspension needs to be diluted. Due to the dilution, important information regarding the stability of the suspension can be lost.

Figure 1 shows information regarding the stability of the concentrated suspension of 5SmHAp obtained by the ultrasound measurements. The digitalised ultrasonic signals are recorded on the digital oscilloscope at a very precise interval of 5.00 s (Figure 1a). The peak amplitudes evolve in time in an unusual way for this suspension, compared to many others studied previously. There is an initial slowly decreasing amplitude, followed by a rising amplitude after 2400 s and a hyperpolic decreasing amplitude up to the end of the experiment (5000 s). Time delays between the first echo that was recorded in the analyzed suspension and the equivalent echo in the reference fluid, allowed a precise determination of the velocity of ultrasounds through the sample, for each signal that was recorded. The result for the velocity in the reference fluid was $c_0 = 1478.27$ m/s while the velocity in the analyzed sample was $c = 1492.07$ m/s and the temperature at which the experiment was performed was 23.3 °C. The ultrasound velocity in the sample is very close to the velocity in pure water and has a negligible variation during the experiment. To characterize the evolution in time of the sample's stability the evolution of amplitude in time was also evaluated (Figure 1b). The amplitude of the first echo was the only one measured with sufficient accuracy. The parameter that gives quantitative information on the stability of the suspension is closely related to the slope of the amplitude of the first echo vs. time. The value of the stability parameter computed by the algorithm was $s = \frac{1}{A_m}\left|\frac{dA}{dt}\right| = 1.3 \times 10^{-4} \cdot s^{-1}$, in which A_m is the averaged amplitude of the signals. Ignoring the local maximum at $t = 2400$ s, the overall stability parameter can be estimated as $s = 9 \times 10^{-4} \cdot s^{-1}$. The value obtained for the stability parameter shows a very good stability of 5SmHAp concentrate suspension.
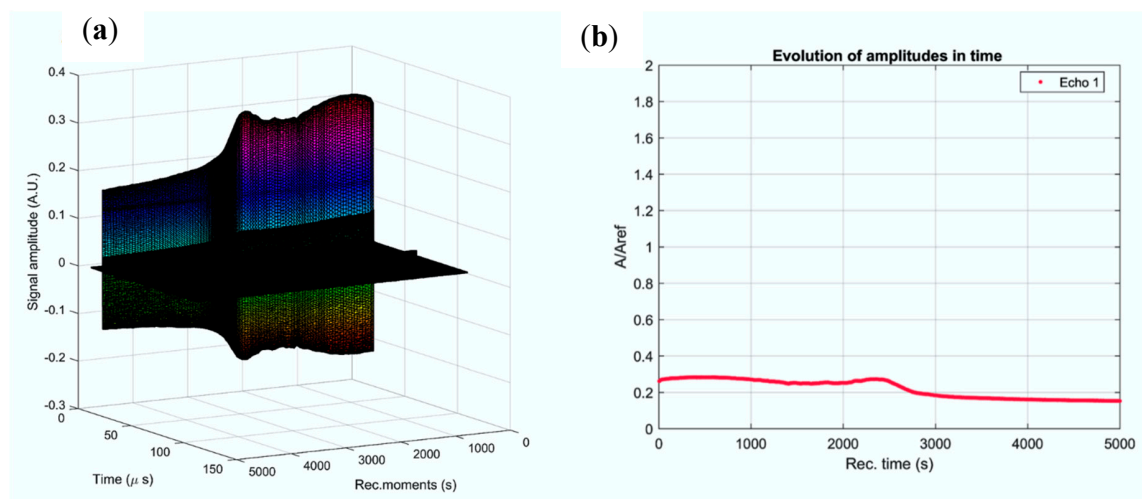
Figure 1. (**a**) Recorded signals at 5 s recording interval. A decreasing amplitude of the first echo is visible in colors, whereas the second is significantly weaker (in black); (**b**) Relative amplitudes evolution vs. the recording moments (**a**).

The relative spectral amplitude vs. time for the first echo and attenuation vs. time for the spectral components of echo 1 revealed the complex information concerning the stability of the analyzed concentrated suspension (Figure 2). Figure 2a shows the initial highest amplitude ratio of 0.55 for the frequency of 2 MHz and the lowest of 0.25 at 8 MHz. For accuracy, all values obtained are relative to the values of the reference fluid (double distilled water) measured under the same conditions. Before the peak at value of time $t = 2400$ s, the amplitudes at all selected frequencies are slowly decreasing. After the peak, the amplitudes decrease continuously, which is atypical for a dispersion after 5000 s. It can be expected that after a much longer period, the relative amplitudes will tend to 1, when most of the particles will settle at the bottom of the container. As shown in Figure 2b, the attenuation calculated for each spectral component depends on the moment during the experiment. The HApSm5 has extremely high attenuations from the first moment, between 20 nepper/m for the 2 MHz component, up to 69 nepper/m for the 8 MHz component of the ultrasonic signal. After the localized reduction of

attenuation at $t = 2400$ s, follows a pronounced and continuous increase of the attenuation. The 2 MHz component reaches 28 nepper/m, whereas the 8 MHz component reaches 110 nepper/m. This increase of the attenuation is attributed to the increase of particles concentration during the sedimentation process. The progressive variation of the attenuation with frequency is normal for suspensions of particles which do not resonate at frequencies in the range of the selected transducer.

(a)

(b)
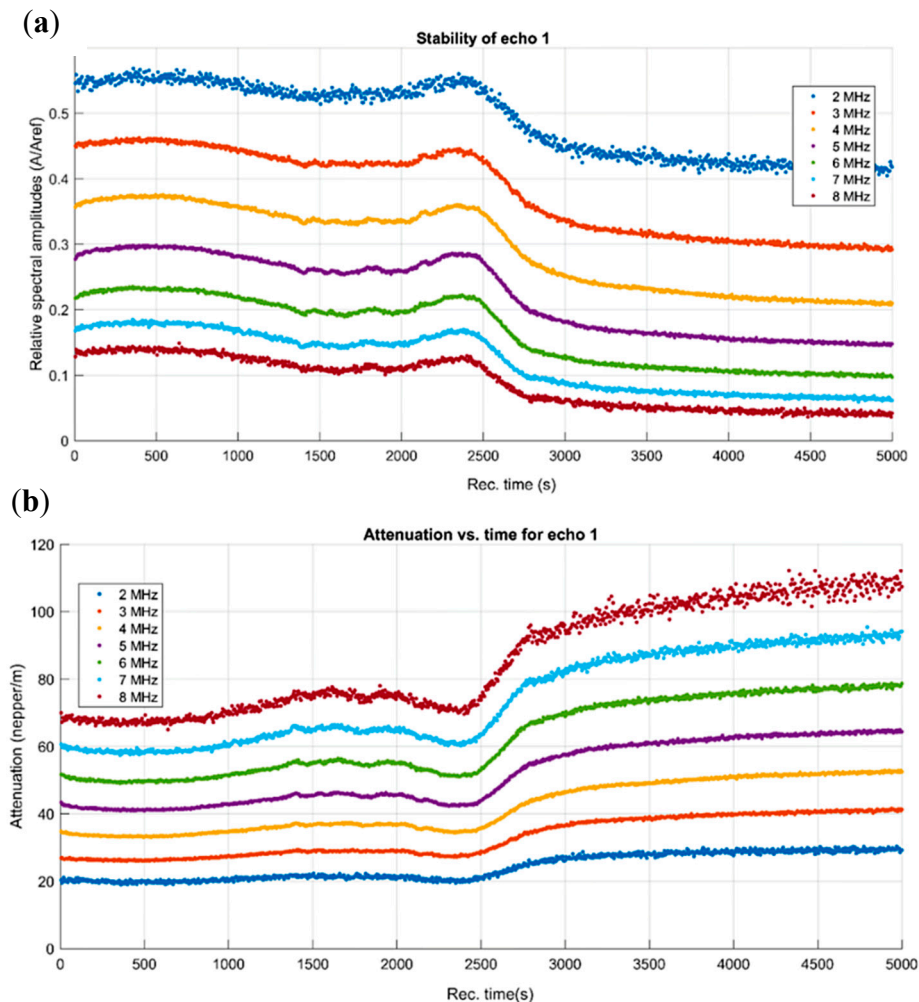
Figure 2. Spectral amplitudes relative variation vs. time, for the first echo (**a**); Attenuation vs. time for the spectral components of echo 1 (**b**).

The morphology of the HAp and 5SmHAp suspension was investigated through TEM and SEM studies. The results of these studies for the HAp suspension are depicted in Figure 3a,b. Also, in Figure 4a,b are presented the SEM and TEM micrographs obtained on the 5SmHAp suspension. In addition, the particle size distribution obtained from TEM and SEM measurements are presented in Figure 3c,d for HAp suspension and in Figure 4c,d for the 5SmHAp suspension.
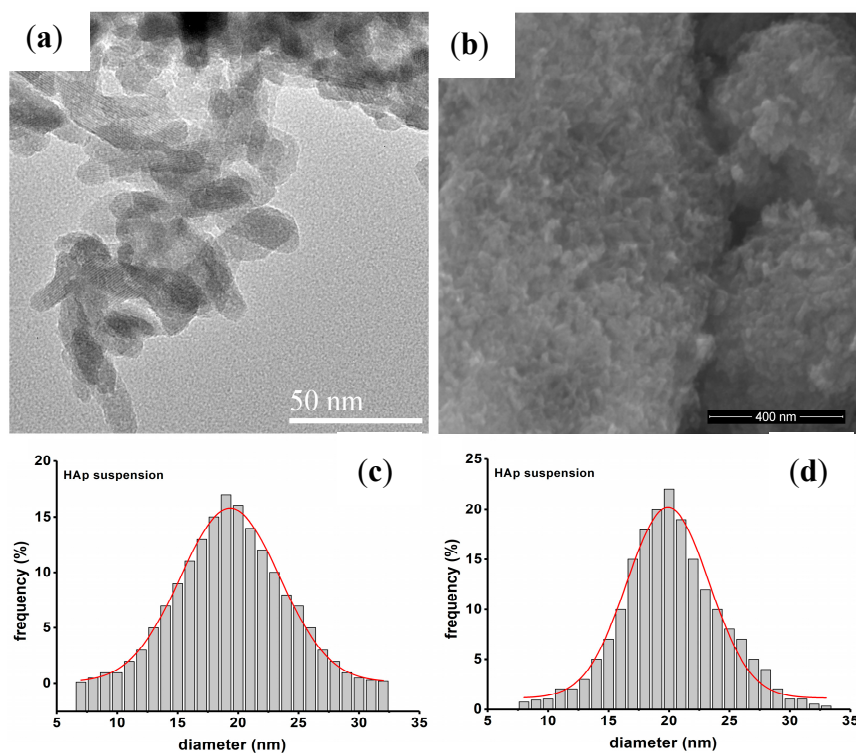
Figure 3. Transmission electron microscopy (TEM) (**a**) and scanning electron microscopy (SEM) (**b**) micrographs of HAp suspension. Particle size distribution of HAp suspension obtained by TEM (**c**) and SEM (**d**) studies.
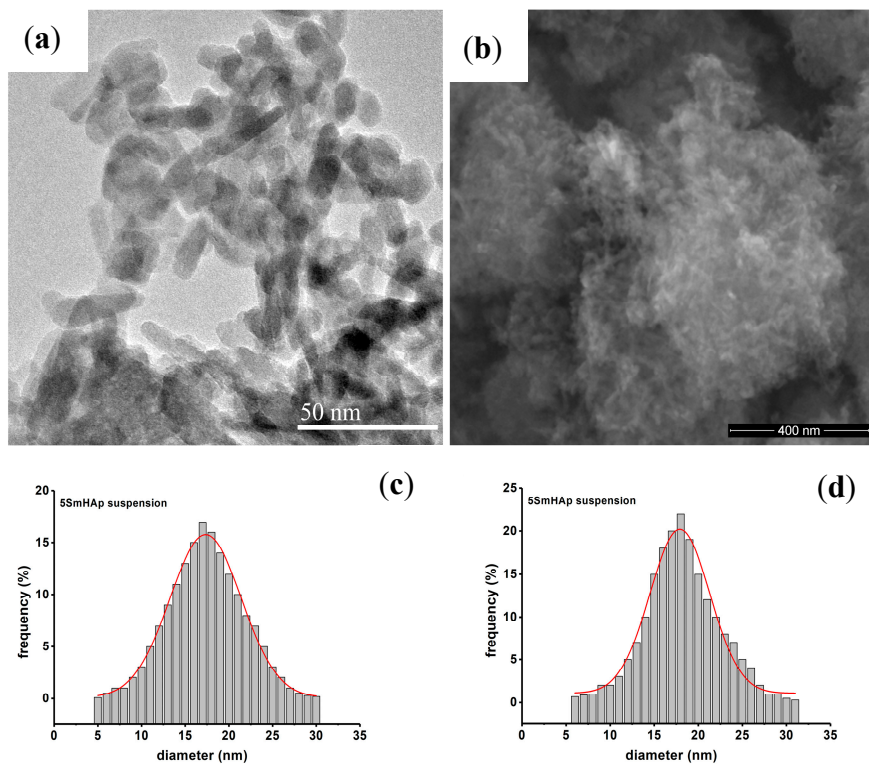

Figure 4. TEM (**a**) and SEM (**b**) micrographs of 5SmHAp suspension. Particle size distribution of 5SmHAp suspension obtained by TEM (**c**) and SEM (**d**) studies.

In the TEM micrographs (Figures 3a and 4a) it could be observed that the HAp and 5SmHAp suspensions consists of particles with nanometric dimensions and ellipsoidal morphology. The mean particle size estimated by TEM studies is around 19 nm in the case of 5SmHAp suspension and about 17 nm for the 5SmHAp suspension. Also, could be noticed that the presence of the samarium in the sample induces a slight decrease of particle size.

The results of the SEM investigations conducted on the HAp and 5SmHAp suspensions presented in Figures 3b–d and 4b–d revealed that for the both samples the nanoparticles tend to agglomerate and exhibit an elongated morphology. Furthermore, the mean particle size obtained by SEM studies was around 20 nm for the 5SmHAp suspension and about 18 nm for the 5SmHAp suspension. Therefore, it can be seen that the results of SEM studies are in good agreement with those obtained through TEM studies.

FTIR measurements were conducted in order to investigate the presence of the vibrational bands characteristic to the HAp structure in the samples. In Figures 5 and 6 are presented the general FTIR absorbance spectra of HAp and 5SmHAp coatings and suspension along with their FTIR deconvoluted spectra in the 400–700 cm^{-1} and 900–1200 cm^{-1} spectral regions.
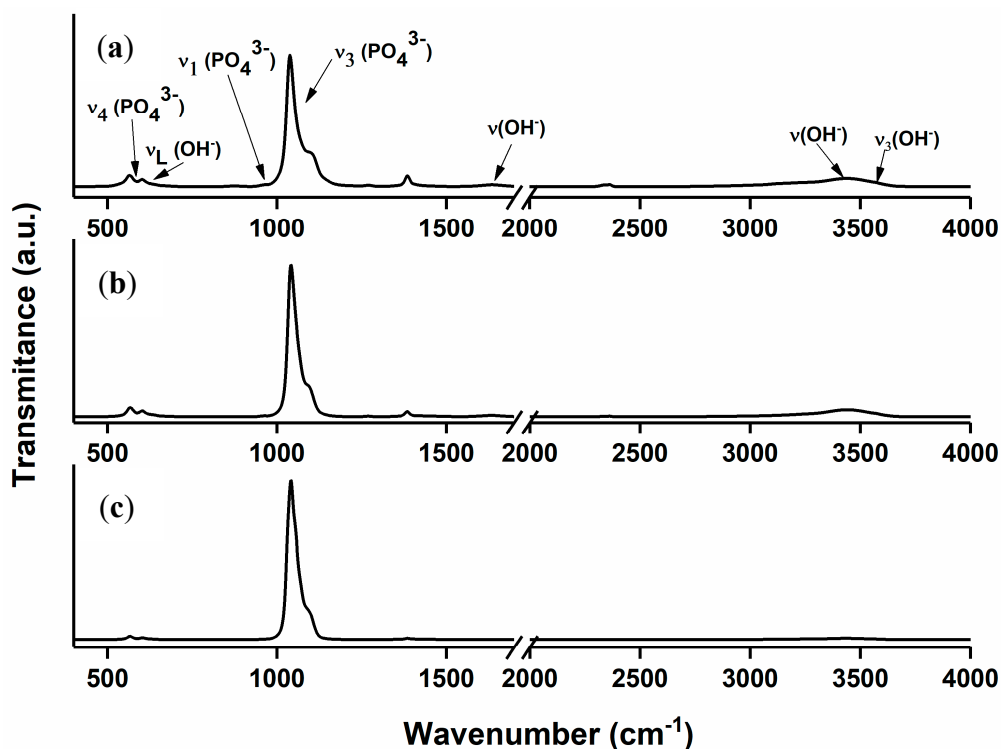
Figure 5. Fourier transform infrared (FTIR) absorbance spectra for HAp suspension (**a**) and 5SmHAp suspension (**b**) and coatings (**c**).
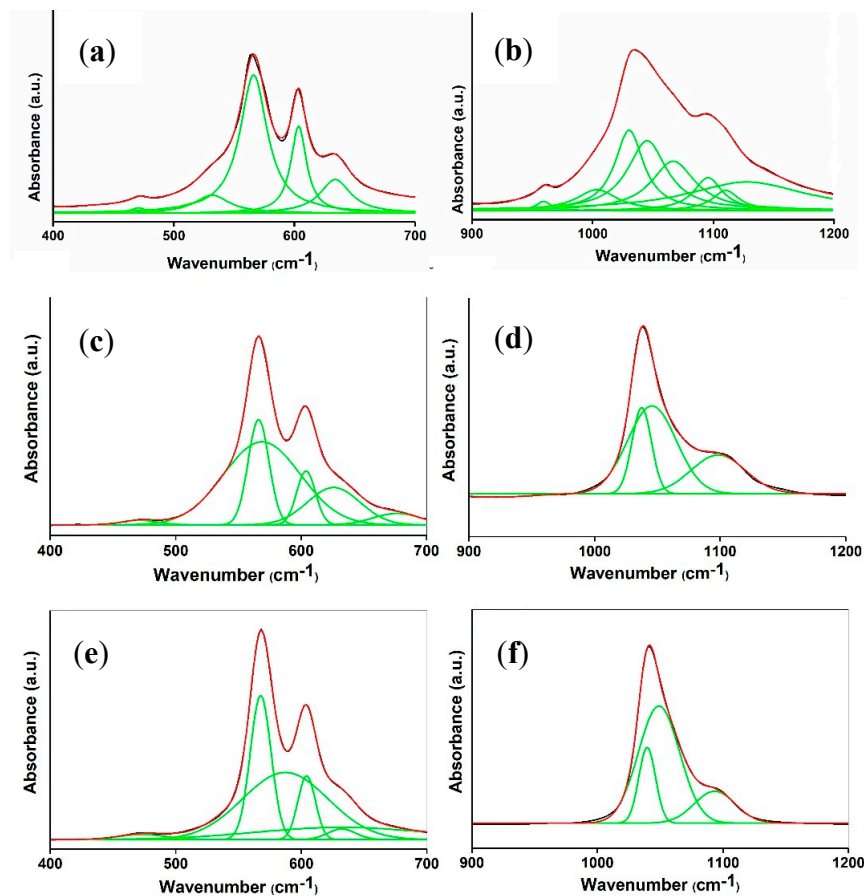
Figure 6. FTIR deconvoluted spectra in the 400–700 cm^{-1} and 900–1200 cm^{-1} spectral regions for HAp suspension (**a,b**) and 5SmHAp suspension (**c,d**) and coatings (**e,f**).

In the general FTIR absorbance spectra (Figure 5) of the studied samples have been identified the peaks belonging to the main vibrational modes of the adsorbed water (H–O–H), phosphate (PO$_4^{3-}$) and hydroxyl (OH$^-$) groups characteristic of the hydroxyapatite structure. The presence of the peak at about 635 cm^{-1} corresponds to the stretching librational mode (v_L) of (OH$^-$) group [35,36]. At the same time, the presence of the peak at around 3570 cm^{-1} is due to stretching mode of (OH$^-$) groups. The presence of wide peaks in the 1600–1700 cm^{-1} and 3200–3600 cm^{-1} spectral regions are assigned to H–O–H bands of lattice water [35–37]. The presence of the peaks at around 1045 and 1093 cm^{-1} denote the presence of v_3 of (PO$_4^{3-}$) group [35,36]. Furthermore, the peaks at around 604 and 568 cm^{-1} belong to v_4 of (PO$_4^{3-}$) group. In agreement with the studies conducted by Iconaru et al. [35] a well crystalized hydroxyapatite structure is highlighted by the presence of the vibrational bands at around 635 cm^{-1} and at about 3570 cm^{-1} (which correspond to the OH$^-$ groups from the structure of hydroxyapatite). On the other hand, it can be seen that the vibration bands are more intense in the case of 5SmHAp coatings compared to HAp and 5SmHAp suspensions. This behaviour is atributed to the the fact that the 5SmHAp coatings are more crystaline comparative to the other two studied samples. Also, in the case of 5SmHAp coatings a slight displacement of the position of the peaks was observed.

Figure 6 depicts the deconvoluted FTIR spectra of the HAp suspension 5SmHAp coatings and suspension (green lines represents the individual subbands) in the 400–700 cm^{-1} and 900–1200 cm^{-1} spectral regions. In Figure 6a,b it can be observed that in order to obtain a good fit of the experimental data obtained oh HAp suspension, five subbands are needed in the spectral region 450–700 cm^{-1}, while for the spectral domain between 900 and 1200 cm^{-1}, eight subbands are needed. Also, it can be seen that in the case of 5SmHAp coatings in order to obtain a good fitting in the 400–700 cm^{-1} spectral region are needed six main components while for the 900–1200 cm^{-1} spectral region are needed four

main components. In addition, our studies revealed that to have a good fit for the 5SmHAp suspension are needed six main components for the 400–700 cm^{-1} spectral region and four components for the 900–1200 cm^{-1} spectral region. Furthermore, an increase in the intensity of the subbands from the both deconvoluted regions specific to the 5SmHAp coatings could be noticed.This behavior is due to the superior crystallinity of the deposited coatings compared to that of the nanoparticles in suspensions.

In order to analyze the surface chemical elemental composition in the 5SmHAp coatings XPS measurements were conducted. The XPS general spectrum of the coating with $x_{Sm} = 0$ (HAp) and $x_{Sm} = 0.05$ (5SmHAp) was presented in Figure 7. The results indicated that elements such as C, O, Ca, and P were observed in the scan of HAp and 5SmHAp general spectrum (Figure 7a,b). In the scan of 5SmHAp XPS general spectra Sm was observed, too.
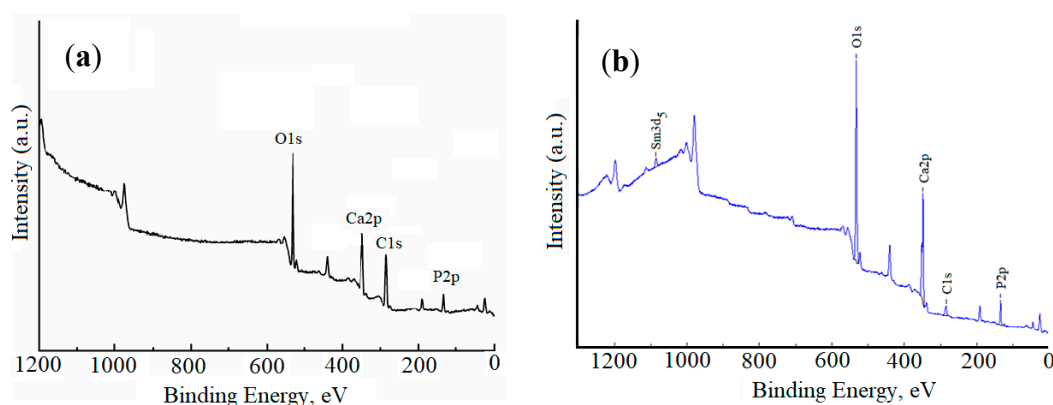
Figure 7. X-ray photoelectron spectroscopy (XPS) general spectrum of the coating with (**a**) $x_{Sm} = 0$ (HAp) and (**b**) $x_{Sm} = 0.05$ (5SmHAp).

The high resolution of C 1*s*, Ca 2*p*, O 1*s*, P 2*p* and Sm 3*d* are exhibited in Figure 8. The high-resolution C 1*s* spectra for the coating with $x_{Sm} = 0$ (HAp) and $x_{Sm} = 0.05$ (5SmHAp) are presented in Figure 8a,b. The peak in the C 1*s* region for HAp coating presented one component of the binding energy (BE) of 284.8 eV attributed to C–C bonds was used as a reference (Figure 8a). Three peaks in the binding energy (BE) region of C 1*s* were observed (Figure 8b). The peak of C 1*s* at 284.8 eV attributed to C–C bonds was used as a reference. Peak of C 1*s* at 286.74 eV can be assigned to C–O bonds while peak at 289.63 eV can be assigned to C=O bonds. In Figure 8c,d the high-resolution Ca 2*p* spectra for HAp and 5SmHap coatings is presented. The peaks in the BE region of Ca 2*p* exhibits a well-defined doublet with two components (Ca 2*p*3/2 and Ca 2*p*1/2). For the 5SmHAp coatings the BE shift slightly from 347.2 eV (for the HAp coatings) to 347.8 eV for the 5SmHAp coatings. The peak located at about 347.2 eV highlights that the calcium atoms are bound to a phosphate group (PO$_4^{3-}$). Kaciulis et al. showed [38] that the shift of the maximum to a higher value of the binding energy in the case of hydroxyapatite doped with different ions shows that the obtained sample is well crystallized. The high resolution XPS spectra of oxygen O 1*s* for pure HAp ($x_{Sm} = 0$) coating was shown in the Figure 8e. The peak at BE of 531.4 eV was assigned to hydroxyl groups that are the result of water or oxygen chemisorption [39]. The O 1*s* photoelectron peak was deconvoluted into two components (Figure 6f). The component located at 531.4 eV is characteristic to O 1*s* peak in HAp structure while the peak at 534.1 eV was attributed to the O 1*s* in adsorbed water [40,41]. The second component of O 1*s* was observed in the coatings obtained by sol-gel method [38,41]. In previous studies, Gaggiotti et al. [42] reported that the EB = 531.8 eV correspond to a position of the hydroxyl ion (OH$^-$). Kawabe et al. [43] appreciate that the two oxygen species (O– and OH), may be attributed to the peak at binding energy of 531.2 eV. Moreover, according to previous studies [44–46] the peak position of chemisorbed oxygen species O– could be attributed to a binding energy between EB = 531.0–531.5 eV. The P 2*p* photoelectron peak of pure HAp coating is shown in Figure 8g. The peak associated to P 2*p* revealed one component after the deconvolution data processing that was located at around EB = 133.1eV. The peak pf P 2*p* of 5SmHAp

coating (Figure 8h) was deconvoluted into two components at 133.01 and 134.04 eV BE in agreement with previous studies [47].
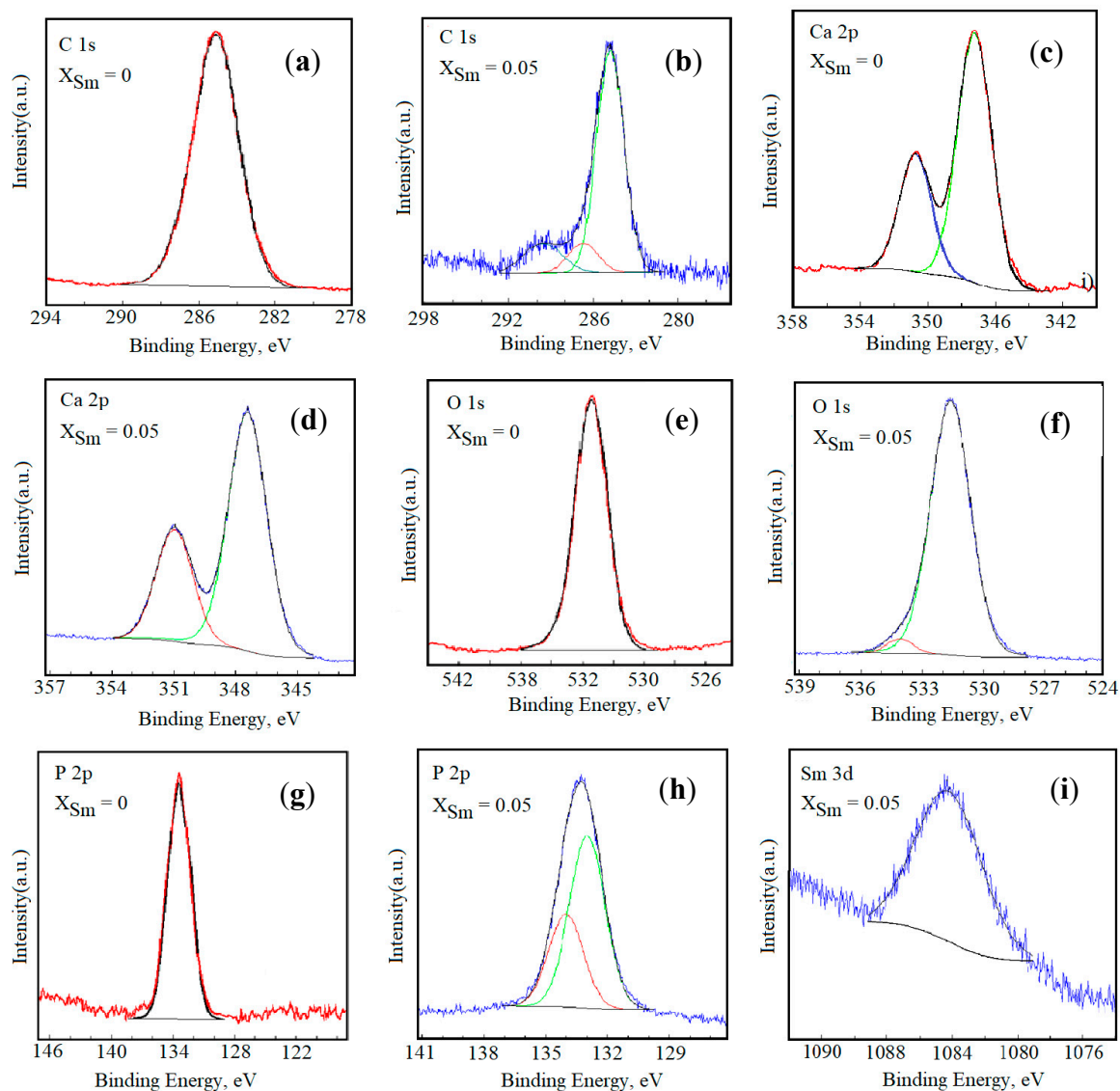

Figure 8. Deconvolution of XPS peaks of C 1*s*, O 1*s*, Ca 2*p*, P 2*p* and Sm 3*d* for the pure HAp (**a,c,e,g**) and 5SmHAp (**b,d,f,h,i**) coatings.

Previous studies on hydroxyapatite layers [48] revealed that the P 2*p* photoelectron line consists of a single component assigned to a peak at binding energy of 133.4 eV. On the other hand, the precedent XPS analysis [49] indicated that the binding energy of the photoelectron peaks for P and Ca are characteristic to their full oxidation states (P^{5+} and Ca^{2+}) for hydroxyapatite. The high resolution spectra of the Sm 2*p*3 is shown in Figure 8i. The peak corresponding to the binding energy of 1082.93 eV can be assigned to Sm 3*d*5/2 [50]. In agreement with previous studies [51], the binding energy of Sm 3*d*5/2 as revealed in Figure 8i suggested that the chemical state of Sm is +3. The XPS results provided obvious information for the successful doping of HAp with samarium.

Figure 9 shows the XRD diffractogram and SEM micrograph of HAp (a,c) and 5SmHAp coatings (b,d). The elemental mapping analysis of the chemical constituents of 5SmHAp coatings (Ca (a), O (b), P (c), Sm (d)) is also presented in Figure 10. In the SEM micrograph (Figure 9d) obtained on the 5SmHAp coatings could be noticed that the surface of the coatings is uniform and continuous with a granular morphology (granules formed by agglomeration of nanoparticles).
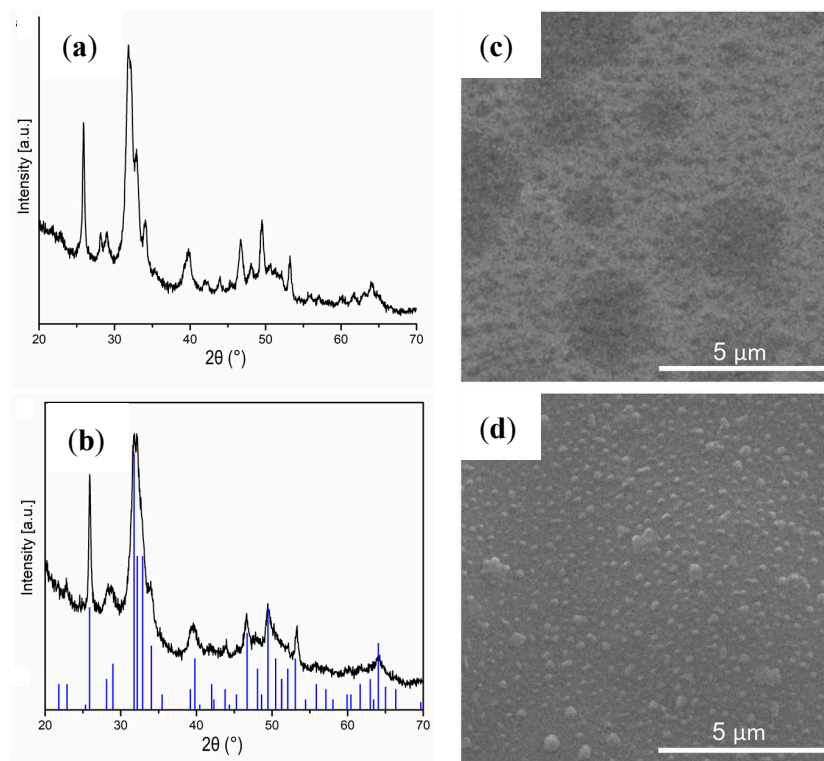
Figure 9. X-ray diffraction (XRD) diffractogram and SEM micrograph of HAp (**a**,**c**) and 5SmHAp coatings (**b**,**d**).
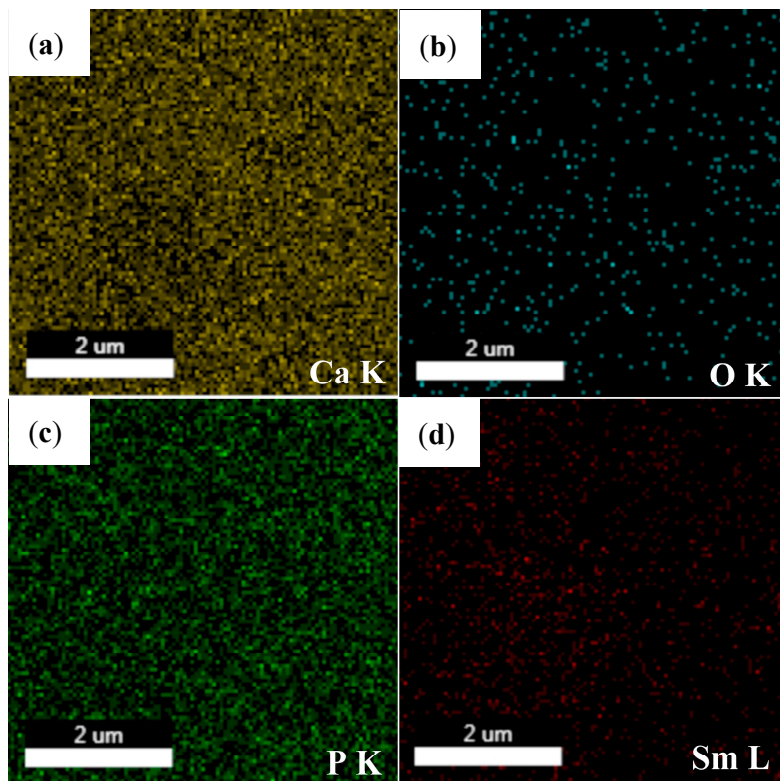

Figure 10. Elemental mapping analysis of the chemical constituent of 5SmHAp coating (Ca (**a**), O (**b**), P (**c**), Sm (**d**)).

In order to determine the crystal structure phase of HAp and 5SmHAp coating, the X-ray diffraction (XRD) was performed using Cu Kα radiation (λ = 1.5406 Å). The XRD patterns of the HAp coating were presented in Figure 9a. Figure 9b shows the XRD patterns of the 5SmHAp coating with x_{Sm} = 0.05. The XRD peaks were indexed by the hexagonal phase of pure hydroxyapatite (JCPDS no. 09-0432). It should be noted that no other secondary phases due to Sm^{3+} ions doped hydroxyapatite were observed after the analysis. This result highlights that Sm^{3+} ions substituted Ca^{2+} ions of 5SmHAp without changing the crystal structure. The diffraction peaks of HAp and 5SmHAp coating correspond to (002), (210), (211), (310), (202), (310), (311), (113), (222), (213), and (004) crystal planes of the hexagonal phase of pure HAp. The average crystallite sizes of the HAp and 5SmHAp coating calculated using Scherrer's formula was around 18 and 15 nm, respectively

On the other hand, in the SEM image of HAp and 5SmHAp coatings (Figure 9c,d) the presence of cracks or fissures on the surface of the coatings could not be observed. The results of the elemental mapping analysis of the chemical constituents of 5SmHAp coatings are presented in the (Figure 10a–d). In the Figure 10a–d can be seen that the main chemical constituents of the 5SmHAp coatings were Ca, O, P, and Sm. Moreover, our studies revealed that all the chemical constituents were evenly distributed in coatings.

The morphology of the HAp and 5SmHAp coatings surface topography has been investigated using atomic force microscopy. The results of the AFM investigations regarding the surface morphology of the HAp and 5SmHAp coatings are depicted in Figure 11a–d.
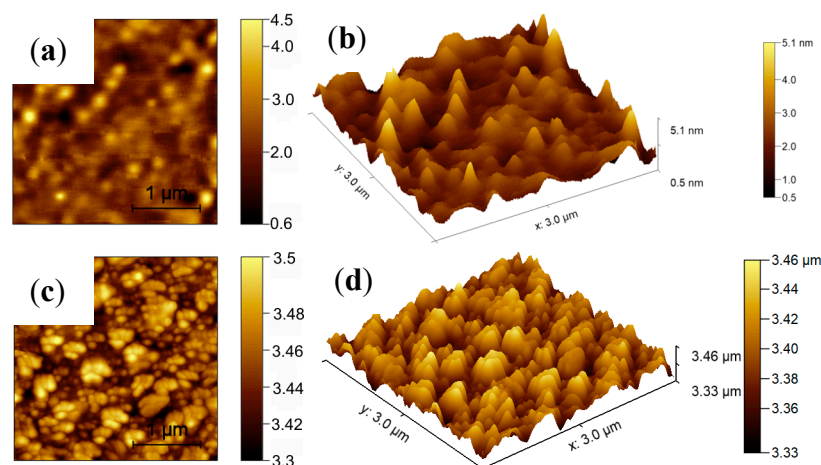

Figure 11. Characteristic 2D atomic force microscopy (AFM) image of HAp (**a**) and 5SmHAp coatings (**c**) and 3D representation of the HAp (**b**) and 5SmHAp (**d**) coatings surface collected on an area of 3×3 μm^2.

Figure 11 presents the AFM 2D micrograph and the 3D representation of the HAp and 5SmHAp surface topography of the HAp and 5SmHAp coatings. The results of the AFM studies emphasized that all the investigated coatings have the morphology of a uniformly deposited layer. Furthermore, the 2D representation of the surface highlighted that there is no visible evidence of the existence of cracks or fissures and that the deposited coatings both in the case of HAp and 5SmHAp samples consist of uniformly distributed nanoaggregates. The AFM results showed that the surface topography of the 5SmHAp coatings was also homogenous having a roughness (R_{RMS}) value of 21.45 nm. In addition, the roughness (R_{RMS}) value for the HAp coatings resulted from the AFM studies was 12.55 nm. The results obtained by AFM studies are in good agreement with the SEM studies, which also revealed that the coatings are uniform and homogenous.

The adhesion of the *C. albicans* cells on the surface of 5SmHAp coatings was also investigated by AFM studies. For this purpose, the surface of HAp and 5SmHAp coatings incubated with *C. albicans* fungal cells at three different time intervals was studied using AFM topography. The results of the AFM

surface topography of the HAp and 5SmHAp coatings incubated with *C. albicans* fungal cells for 24, 48, and 72 h are presented in Figure 12. The 2D AFM images of the 5SmHAp coatings surface highlighted that the *C. albicans* cell development was inhibited by the coatings and that the inhibition rates were correlated with the incubation time. The AFM images collected on an area of 20×20 μm^2 evidenced that the *C. albicans* development was inhibited starting from 24 h and the inhibition continued and accentuated after 48 and 72 h. In the case of the coatings incubated for 72 h, the *C. albicans* cells were almost completely eradicated from the surface of the 5SmHAp coatings, demonstrating that the incubation time strongly affected the antifungal properties of the 5SmHAp coatings. Furthermore, the AFM images of the HAp coatings incubated with *C. albicans* fungal cells emphasized that the HAp coatings promoted the development of the fungal cells and provided a good adhesive surface for the *C. albicans* cells and allowed the development of fungal biofilm.
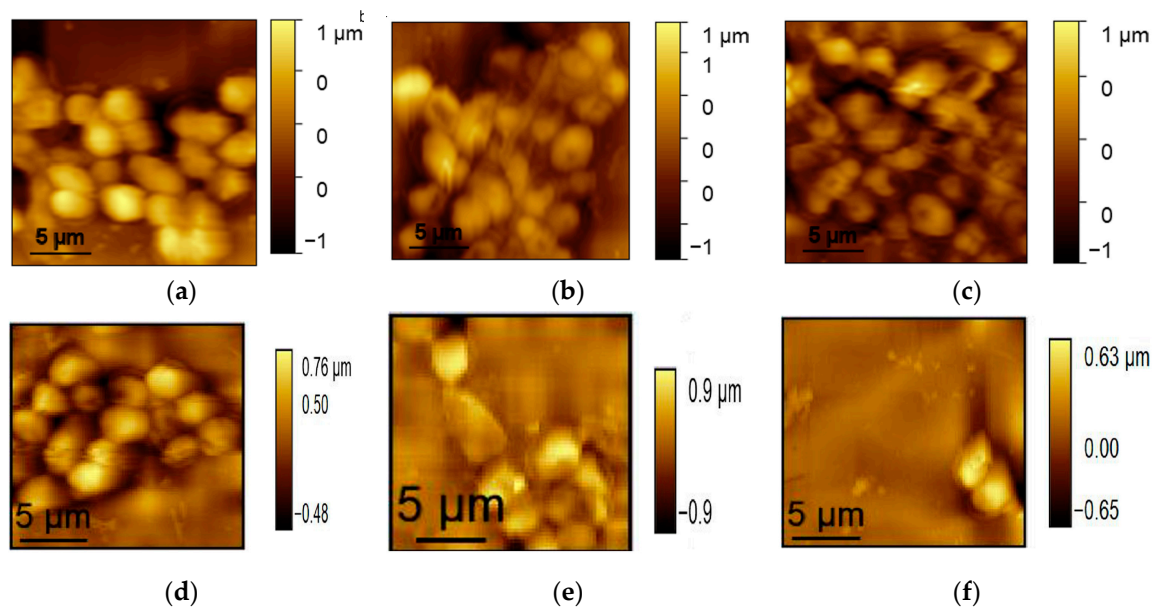
Figure 12. AFM surface topography of *Candida albicans* ATCC 10231 cell development on HAp (**a**–**c**) and 5SmHAp coatings (**d**–**f**) at different time intervals of incubation collected on an area of 20×20 μm^2.

The effects of the 5SmHAp coatings on the adhesion and proliferation of *C. albicans* were furthermore studied using SEM and CLSM investigations. The images of *C. albicans* cell development on the surfaces of 5SmHAp coatings after 24, 48, and 72 h of incubation with the *C. albicans* microbial cells, resulted from SEM observations were presented in Figure 13. The SEM visualization of the 5SmHAp coatings incubated with the fungal cell at different time intervals highlighted that the morphology of the fungal cells was typical to that of the *C. albicans* fungal strain, having round and oval shapes. Moreover, the SEM images emphasized that the size of the *C. albicans* fungal cells were in the range of 2.378–4.419 μm. In addition, the SEM analysis revealed that the fungal cells adhesion and development of biofilms on the 5SmHAp coatings was inhibited only after 24 h of incubation. Moreover, the SEM observations highlighted the inhibitory effects of the 5SmHAp coatings against *C. albicans* fungal strain at all tested time intervals. Furthermore, the results of the SEM visualization evidenced that the inhibitory effect of the 5SMHAp coatings was correlated with the incubation time.
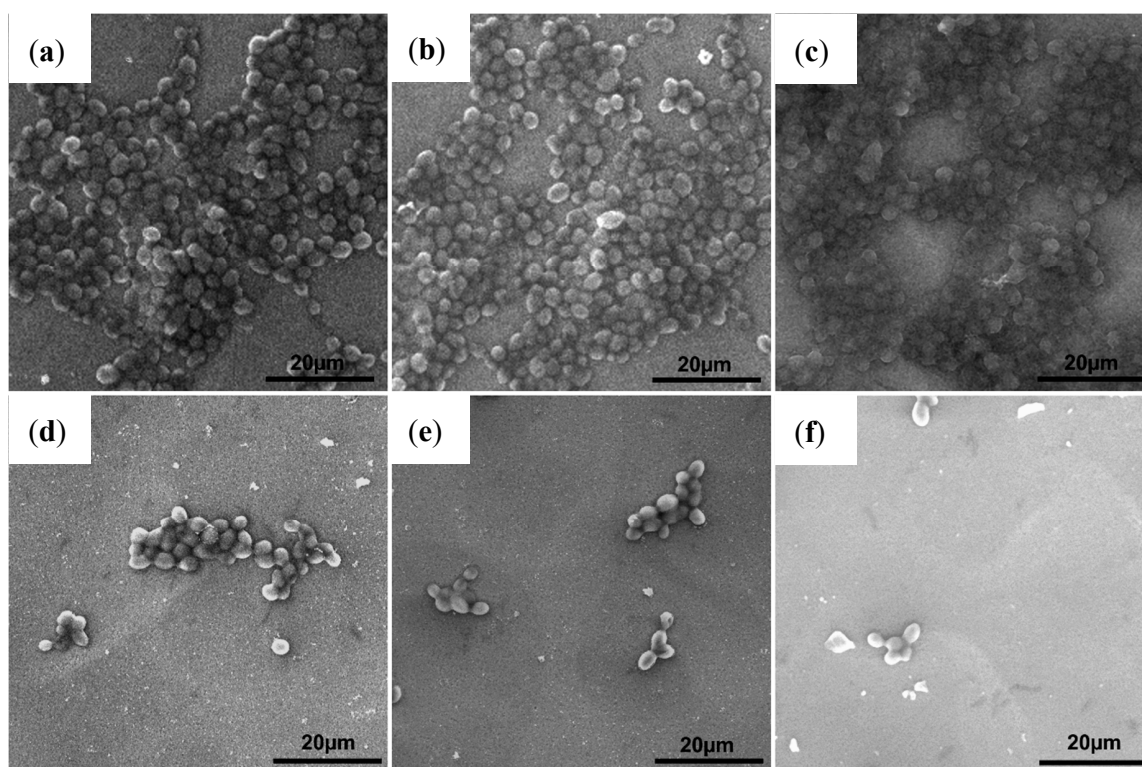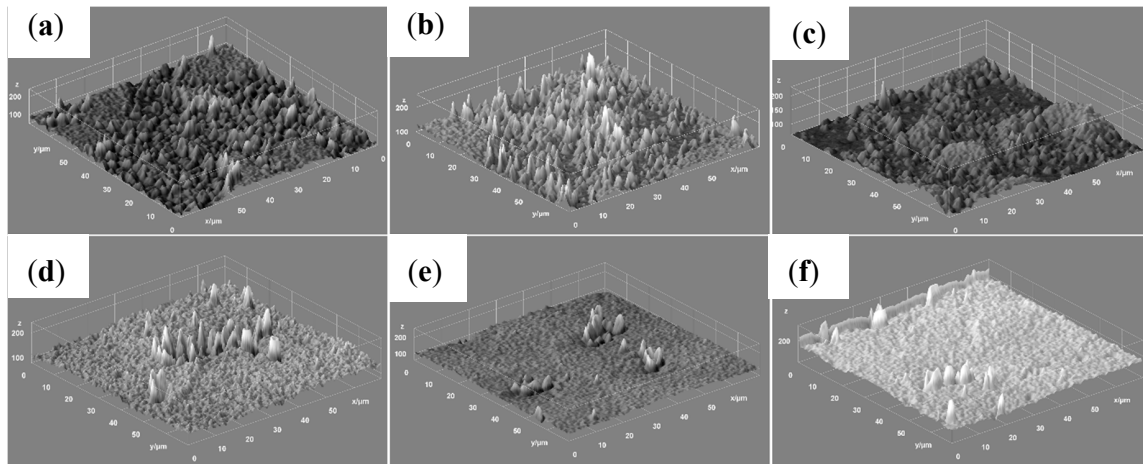
Figure 13. SEM images of *Candida albicans* ATCC 10231 cell development on HAp (**a**–**c**) and 5SmHAp coatings (**d**–**f**) at different time intervals of incubation 24 h (**a**,**d**) 48 h (**b**,**e**) and 72 h (**c**,**f**).

In addition, the *C. albicans* development on the HAp coatings was also assessed by SEM visualization at three different time intervals. The results emphasized that the HAp coatings promoted the development of the fungal cells and aided their proliferation and also allowed the formation of a fungal biofilm on their surface. These studies are in good agreement with previous conducted studies regarding the antifungal properties of HAp. The SEM images have revealed that the number of *C. albicans* fungal cells was considerably diminished after 48 and 72 h of incubation with the 5SmHAp coatings. Furthermore, the 3D representation of the SEM images with the *C. albicans* attached fungal cells was also performed using Image J software (Image J 1.51j8) [33]. The 3D representation of the SEM images of the 5SmHAp coatings incubated at three different time intervals with *C. albicans* fungal cells are presented in Figure 14.

The development and adhesion of *C. albicans* cells on the surface of 5SmHAp coatings after different time incubation intervals were also examined by CLSM. The images acquired using CLSM proved much more clearly, that the *C. albicans* cells development was inhibited by the 5SmHAp coatings and that the coatings did not allowed the fungal cells to proliferate and develop biofilms. These results are in good agreement with previous reported studies regarding the fungal properties of other biocomposite layers deposited on Si and Ti substrates [12,29,52,53]. CLSM is an optical imaging technique and a useful tool for imaging, qualitative analysis and quantification of cells [54,55]. Figure 15 shows the CLSM images of *C. albicans* cell growth on 5SmHAp coatings incubated with the fungal cells at different time intervals. The CLSM visualization was done using propidium iodide to label the fungal cells. The CLSM visualization evidenced that the surviving *C. albicans* cells were intact with round morphology and a smooth surface for all tested time intervals of incubation on the surface of HAp and 5SmHAp coatings. The results are depicted in Figure 15a–f. Furthermore, the CLSM examination confirmed the results obtained by the qualitative antimicrobial assay and was in good agreement with the results obtained from the SEM analysis. CLSM images highlighted that 5SmHAp coatings after 24 h of incubation exhibited a strong antifungal activity against *Candida albicans* ATCC

10231 and inhibited the biofilm formation. In addition, the results obtained by CLSM studies have emphasized that the time of incubation influenced the antifungal activity of the 5SmHAp coatings. The antifungal assays performed revealed that the 5SmHAp coatings could have a great potential to be used in medical application as antifungal coatings for medical devices.
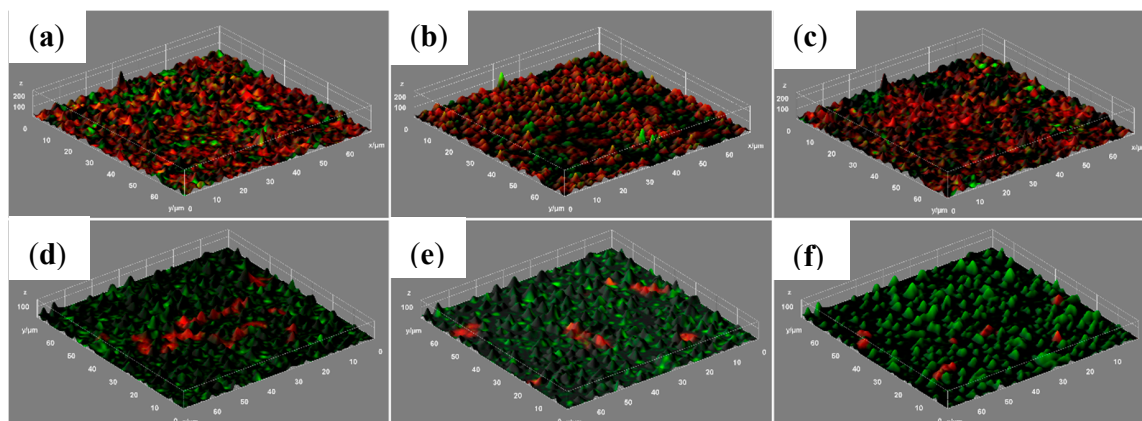

Figure 14. 3D representation of the SEM images of *Candida albicans* ATCC 10231 cell development on HAp (**a**–**c**) and 5SmHAp coatings (**d**–**f**) at different time intervals of incubation 24 h (**a**,**d**) 48 h (**b**,**e**) and 72 h (**c**,**f**).
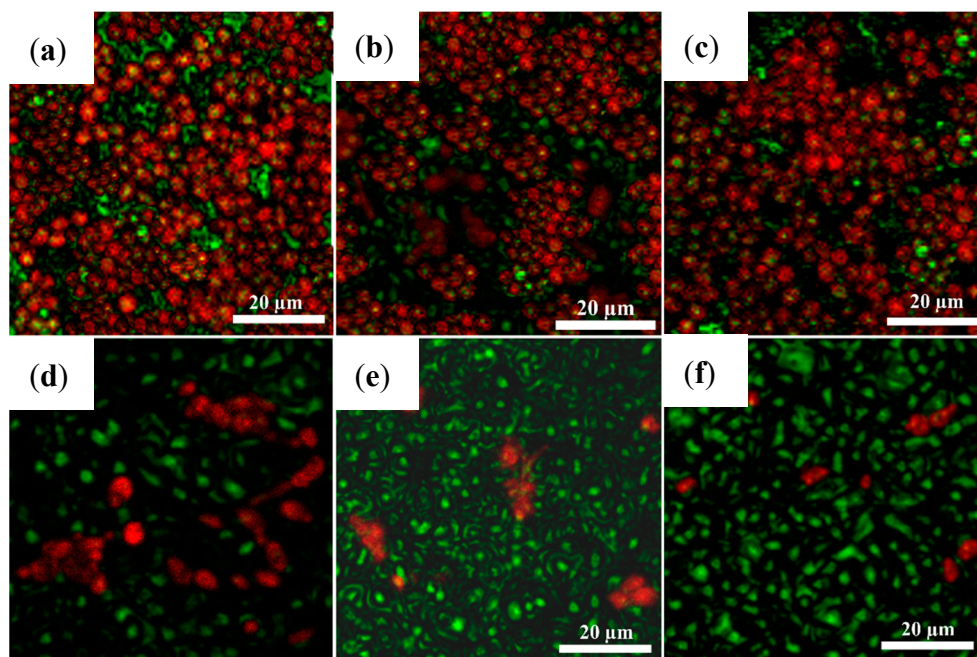
Figure 15. 2D confocal Laser Scanning Microscopy (CLSM) images of *Candida albicans* ATCC 10231 adhesion on HAp (**a**–**c**) and 5SmHAp (**d**–**f**) coatings deposited on Si after 24 h (**a**,**d**), 48 h (**b**,**e**) and 72 h (**c**,**f**) of incubation.

Furthermore, the 3D representation of the CLSM images of *C. albicans* fungal cells adhered on the surface of the 5SmHAp coatings after being incubated at three different time intervals analyzed using Image J software [33] are presented in Figure 16. The 3D representation display the structure and spatial distribution of *C. albicans* surviving cells on the 5SmHAp coatings after 24, 48, and 72 h of incubation with the fungal cells. The images exhibited in Figure 15 revealed the spatial distribution of *C. albicans* surviving cells (red color) along horizontal (coverage) and the vertical (thickness) distributions

on the 5SmHAp surfaces. The CLSM images presented in Figure 16 demonstrated that the survival of *C. albicans* cells have been significantly reduced in the presence of 5SmHAp coatings and that their inhibition was strongly correlated with the incubation time.

Figure 16. 3D representation of the CLSM images of *Candida albicans* ATCC 10231 adhesion on HAp (**a**–**c**) and 5SmHAp (**d**–**f**) coatings deposited on Si after 24 h (**a**,**d**), 48 h (**b**,**e**) and 72 h (**c**,**f**) of incubation.

The quantitative antifungal properties of the HAp and 5SmHAp coatings deposited on silicium substrate were also assessed using *C. albicans* ATCC 10231 fungal strain. The graphical representation of *C. albicans* ATCC 10231 colony-forming units on 5SmHAp suspensions and coatings at three different time intervals (24, 48, and 72 h) are depicted in Figure 17.
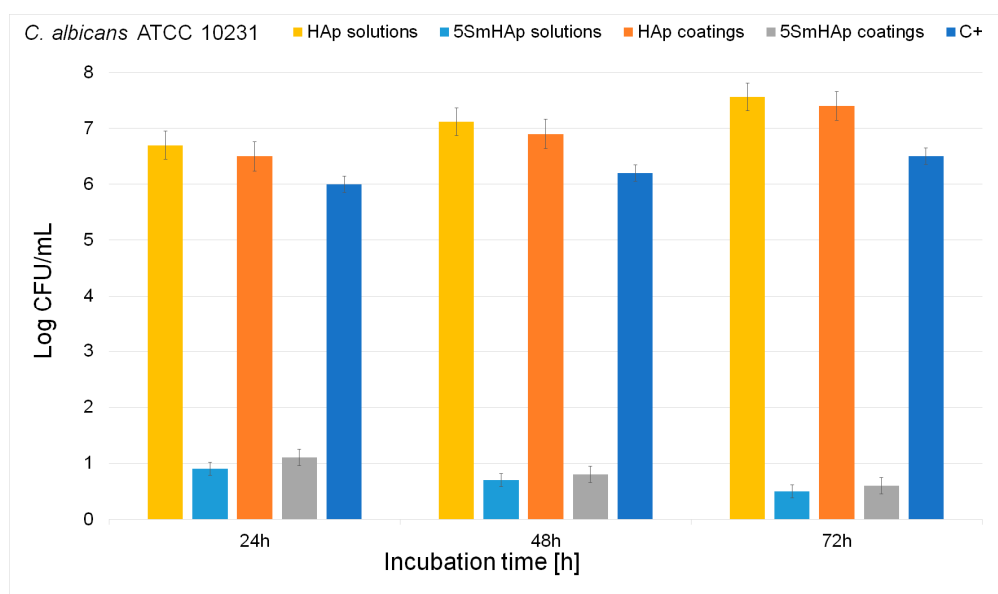
Figure 17. Graphical representation of the Log colony forming units (CFU)/mL of *C. albicans* as a function of time of exposure to the HAp and 5SmHAp suspensions and coatings.

The quantitative results emphasized that the fungal colony forming unity development was inhibited from the early phase of adherence in the case of 5SmHAp both suspensions and coatings. The colony forming unit count (CFUc) assay showed a significant decrease of the number of colonies in the case of both 5SmHAp suspensions and coatings compared to the number of colonies formed in the case of the control culture. Furthermore, the results emphasized that the antifungal activity of 5SmHAp suspensions was higher than that of 5SmHAp coatings for all tested intervals. The results obtained

by the qualitative and quantitative studies conducted, evidenced that the 5SmHAp suspensions and coatings inhibited the *C. albicans* fungal strain development. The results are in good agreement with previous reported data [10,53,56–58] and emphasized that samarium ions exhibit antifungal properties.

The antifungal properties of HAp suspensions and HAp coatings were also investigated and a free *C. albicans* culture was used as positive control C+. The results demonstrated that both HAp suspensions and HAp coatings encouraged the proliferation of the fungal cells and influenced positive their growth for all tested time intervals. These results are in good agreement with previously reported studies regarding the lack of antimicrobial properties of hydroxyapatite [20,59,60]. Moreover, previous studies [15,56–64] reported that the antifungal effect of samarium could be explained by the fact that samarium ions have the ability to attach to the cell membrane leading to changes of its permeability. Furthermore, samarium ions that are released from the composite matrix could disrupt the bacterial membrane integrity thus affecting a multitude of cellular processes such like adhesion, ion conductivity and cell signaling [61].

The results of the qualitative and quantitative antifungal assays are in agreement with the previous data presented in the literature and highlighted that the Sm^{3+} ions present in the hydroxyapatite matrix of the 5SmHAp coatings is responsible for the antifungal activity of the coatings. Moreover, the data also suggested that the antifungal activity of both the 5SmHAp suspensions and coatings are strongly correlated with the incubation time. The qualitative studies conducted by AFM, SEM and CLSM suggested that the adhesion of *C. albicans* fungal cells was greatly reduced by the samarium doped composites. These results are similar with those reported in the literature, regarding the adherence of *S. aureus*, *S. epidermidis* and *P. aeruginosa* strains on composites doped with samarium [15]. The results reported by the authors showed that compared to glass-reinforced hydroxyapatite composites (GR-HA) composite the *S. aureus*, *S. epidermidis* and *P. aeruginosa* microbial cell development was considerably inhibited in the Sm doped composites and that the microbial cell reduction was correlated with the Sm content. The antibacterial effect of the composites were attributed also to the release of samarium ions from the composites. Thus, the development of 5SmHAp coatings with enhanced osteoblastic cell response given by the hydroxyapatite matrix and possessing antibacterial activity due to the presence of samarium ions could lead to a better outcome of bone graft implantation. The choice of Si as a substrate started from the intention to extend the applicability of these biocompatible materials with antimicrobial properties from dental field to devices that could be used in tissue engineering [62] or human prosthetic [63] in order to prevent postoperative infections. Ruffino and Torrisi [64] in their studies regarding the influence of interaction between film and substrate on the nanoscale film morphology showed that between Ag films deposited on SiO_2/Si and TiO_2/Ti substrates exist various differences. Also Jouanny et al. [65] reported that between the TiO_2 thin films deposited on the Si and Ti–6Al–4V substrate respectively, are differences from mechanical point of view. According to the studies reported by Barry et al. [66] the nature of the substrate could influence the surface roughness and coating thickness but there are no significant differences between the interface properties and the coating composition depending on the type of alloy. Moreover, Ferraris et al. [67] reported that the substrate also influences the biological properties of the samples.

Furthermore, due to the intended purpose of being used in biomedical applications, the toxicity of the HAp and 5SmHAp suspensions and coatings were also assessed using one of the most studied cell line. The toxicity of HAp and 5SmHAp suspensions and coatings was assessed against HeLa cells at three different time intervals (24, 48, and 72 h). The results of the cytotoxicity assay obtained by MTT 3-(4,5-dimethylthiazol-2-yl)-2,5-diphenyltetrazolium bromide (MTT) are presented in Figure 18. HeLa cell line is the oldest and the most commonly used human cell line and has been extensively used in scientific studies due to its remarkably durable and prolific properties. Since its discovery, the HeLa cells have been intensively and continually used for research into various fields of research such as cancer, AIDS, the effects of radiation and toxic substances, the toxicity of nanoparticles and other types of materials, gene mapping and countless other scientific pursuits.
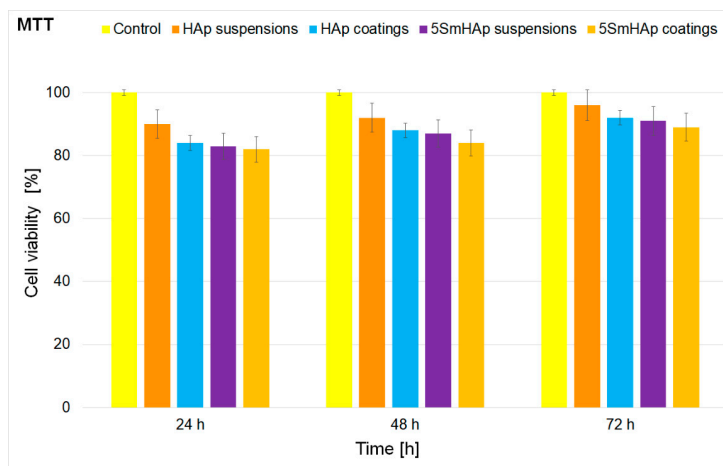
Figure 18. MTT assay for the viability of HeLa cells incubated with HAp and 5SmHAp suspensions and coatings at different time intervals.

The MTT studies revealed that after 24 h of incubation time, there were no representative differences between the cells viabilities of the HAp and 5SmHAp suspensions. The results have emphasized that after 24 h of incubation, the cell viability of HeLa cells was 90% in the case of the HAp suspensions and 84% in the case of the HAp coatings and also 83% in the case of 5SmHAp suspensions and 82% for the HeLa cells incubated with the 5SmHAp coatings. Moreover, the MTT assay results show that after 48 and 72 h of incubation a slight increase of the HeLa cell viability was observed for all the investigated samples.

The results highlighted that there is a correlation between the incubation time and the cell viability of the samples. Moreover, the MTT suggested that the HAp and 5SmHAp suspensions had better biocompatible properties than the HAp and 5SmHAp coatings. The results obtained in the present study are in good agreement with previous studies regarding the toxicity of hydroxyapatite suspensions and coatings [68–70]. In addition, a live/dead cell viability assay was performed in order to quantify the ratio of the live and dead cells after the incubation of the HeLa cells with 5SmHAp solutions and coatings at different time intervals. The results are depicted in Figure 19. The results are in agreement with the MTT assay and evidenced that both the 5SmHAp solutions and coatings did not present any toxicity against the tested cells for all tested time intervals. Furthermore, the data suggested that the percent of dead cells in the case of both samples and for all tested intervals was under 10% from the total number of counted cells.
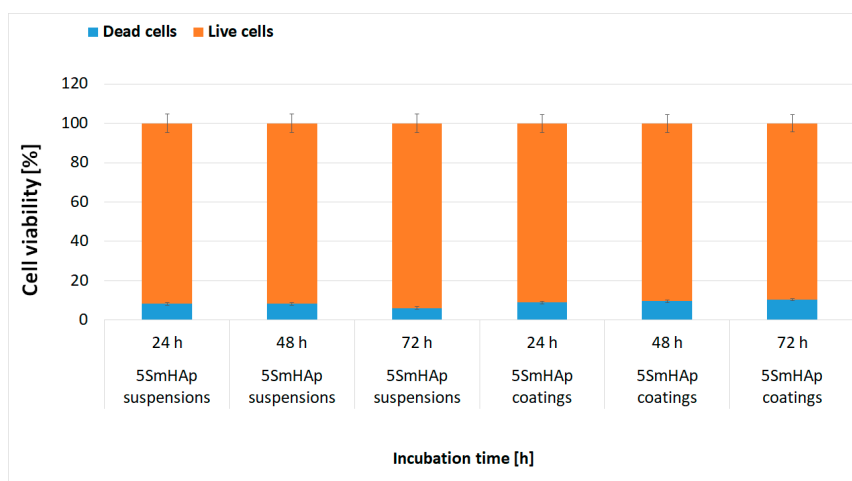
Figure 19. Percent of total counts of live cells and dead cells after incubation with 5SmHAp suspensions and coatings at different time intervals.

4. Conclusions

Hydroxyapatite and samarium doped hydroxyapatite ($x_{Sm} = 0.05$) coatings were synthesized by a simple sol-gel route using the dip coating method. Characterization studies of HAp and 5SmHAp nanoparticles in suspension and coatings using different techniques were performed. The stability of 5SmHAp suspension was highlighted by ultrasound measurements. Ultrasound measurements showed that the 5SmHAp suspension had a behavior similar to that of double-distilled water considered as a reference fluid. XPS and XRD studies on 5SmHAp coating confirmed that the Sm^{3+} ions have been incorporated into the 5SmHAp synthesized material by substituting the Ca^{2+} ions. The uniform distribution of constituent elements on 5SmHAp coating surface was confirmed by elemental mapping analysis. SEM and AFM investigations revealed the uniform and homogenous surface of 5SmHAp coating. In addition, FTIR studies confirmed the presence of the functional groups characteristic to the HAp structure in both samples. The AFM analysis of the surface coatings revealed the obtaining of homogenous and uniform coatings with no cracks or fissures. The antifungal activity of HAp and 5SmHAp coatings and suspensions was investigated using a *Candida albicans* ATCC 10231 fungal strain. The results of the quantitative assay of the antifungal activity revealed that both 5SmHAp coatings and suspensions inhibited the development of *C. albicans* fungal strain. The results obtained by the qualitative assays using AFM, SEM CLSM visualization of the *C. albicans* cell adherence on the surface coatings confirmed the quantitative results and evidenced that the antifungal properties of the coatings were influenced by the incubation time. Furthermore, the cytotoxic assay using HeLa cell line emphasized that both 5SmHAp suspensions and coatings did not present any toxicity against HeLa cells for all tested incubation intervals. Nowadays, following the occurrence of microbial infections affecting public health, the development of novel materials that could be used as a cheap alternative for the obtaining of coatings with high antimicrobial activity over time is of great interest.

References

1. Nabeel, A.I. Samarium enriches antitumor activity of ZnO nanoparticles via downregulation of CXCR4 receptor and cytochrome P450. *Tumor Biol.* **2020**, *42*, 1–14. [CrossRef]
2. Alicka, M.; Sobierajska, P.; Kornicka, K.; Wiglusz, R.J.; Marycz, K. Lithium ions (Li Enhance expression of late osteogenic markers in adipose-derived stem cells. Potential theranostic application of nHAp doped with Li^+) and nanohydroxyapatite (nHAp) doped with Li^+ and co-doped with europium (III) and samarium (III) ions. *Mater. Sci. Eng. C* **2019**, *99*, 1257–1273. [CrossRef]
3. LeGeros, R.Z. Properties of osteoconductive biomaterials: Calcium phosphates. *Clin. Orthop.* **2002**, *395*, 81–98. [CrossRef] [PubMed]
4. Giannoudis, P.V.; Dinopoulos, H.; Tsiridis, E. Bone substitutes: An update. *Injury* **2005**, *36*, S20–S27. [CrossRef] [PubMed]

5. Sathishkumar, S.; Louis, K.; Shinyjoy, E.; Gopi, D. Tailoring the Sm/Gd-substituted hydroxyapatite coating on biomedical AISI 316L SS: Exploration of corrosion resistance, protein profiling, osteocompatibility, and osteogenic differentiation for orthopedic implant applications. *Ind. Eng. Chem. Res.* **2016**, *55*, 6331–6344. [CrossRef]

6. Barroug, A.; Glimcher, M.J. Hydroxyapatite crystals as a local delivery system for cisplatin: Adsorption and release of cisplatin in vitro. *J. Orthop. Res.* **2002**, *20*, 274–280. [CrossRef]

7. Uskoković, V.; Uskoković, D.P. Nanosized hydroxyapatite and other calcium phosphates: Chemistry of formation and application as drug and gene delivery agents. *J. Biomed. Mater. Res. B Appl. Biomater.* **2011**, *96*, 152–191. [CrossRef] [PubMed]

8. Raita, M.S.; Iconaru, S.L.; Groza, A.; Cimpeanu, C.; Predoi, G.; Ghegoiu, L.; Badea, M.L.; Chifiriuc, M.C.; Marutescu, L.; Trusca, R.; et al. Multifunctional hydroxyapatite coated with arthemisia absinthium composites. *Molecules* **2020**, *25*, 413. [CrossRef]

9. Zantyea, P.; Fernandesa, F.; Ramananb, S.R.; Kowshik, M. Rare earth doped hydroxyapatite nanoparticles for in vitro bioimaging applications. *Curr. Phys. Chem.* **2019**, *9*, 94–109. [CrossRef]

10. Turculet, C.S.; Prodan, A.M.; Negoi, I.; Teleanu, G.; Popa, M.; Andronescu, E.; Beuran, M.; Stanciu, G.A.; Hristu, R.; Badea, M.L.; et al. Preliminary evaluation of the antifungal activity of samarium doped hydroxyapatite thin films. *Rom. Biotechnol. Lett.* **2018**, *23*, 13928–13932.

11. Prodan, A.M.; Iconaru, S.L.; Predoi, M.V.; Predoi, D.; Motelica-Heino, M.; Turculet, C.S.; Beuran, M. Silver-doped hydroxyapatite thin layers obtained by sol-gel spin coating procedure. *Coatings* **2020**, *10*, 14. [CrossRef]

12. Predoi, D.; Iconaru, S.L.; Predoi, M.V. Bioceramic layers with antifungal properties. *Coatings* **2018**, *8*, 276. [CrossRef]

13. Predoi, D.; Iconaru, S.L.; Albu, M.; Petre, C.C.; Jiga, G. Physicochemical and antimicrobial properties of silver-doped hydroxyapatite collagen biocomposite. *Polym. Eng. Sci.* **2017**, *57*, 537–545. [CrossRef]

14. Šupová, M. Substituted hydroxyapatites for biomedical applications: A review. *Ceram. Int.* **2015**, *41*, 9203–9231. [CrossRef]

15. Morais, D.S.; Coelho, J.; Ferraz, M.P.; Gomes, P.S.; Fernandes, M.H.; Hussain, N.S.; Santos, J.D.; Lopes, M.A. Samarium doped glass-reinforced hydroxyapatite with enhanced osteoblastic performance and antibacterial properties for bone tissue regeneration. *J. Mater. Chem. B* **2014**, *2*, 5872–5881. [CrossRef] [PubMed]

16. Ciobanu, C.S.; Popa, C.L.; Predoi, D. Sm:HAp nanopowders present antibacterial activity against enterococcus faecalis. *J. Nanomater.* **2014**, *2014*, 780686. [CrossRef]

17. Nakayama, M.; Smith, C.L.; Feltis, B.N.; Piva, T.J.; Tabatabaie, F.; Harty, P.D.; Gagliardi, F.M.; Platts, K.; Otto, S.; Blencowe, A.; et al. Samarium doped titanium dioxide nanoparticles as theranostic agents in radiation therapy. *Phys. Med.* **2020**, *75*, 69–76. [CrossRef]

18. Zhang, Y.; Wang, X.; Su, Y.; Chen, D.; Zhong, W. A doxorubicin delivery system: Samarium/mesoporous bioactive glass/ alginate composite microspheres. *Mater. Sci. Eng. C Mater. Biol. Appl.* **2016**, *67*, 205–213. [CrossRef]

19. Kannan, S.; Nallaiyan, R. Anticancer activity of Samarium-coated magnesium implants for immunocompromised patients. *ACS Appl. Bio Mater.* **2020**, *3*, 4408–4416. [CrossRef]

20. Iconaru, S.L.; Predoi, M.V.; Stan, G.E.; Buton, N. Synthesis, characterization, and antimicrobial activity of Magnesium-doped hydroxyapatite suspensions. *Nanomaterials* **2019**, *9*, 1295. [CrossRef]

21. Ciobanu, C.S.; Iconaru, S.L.; Massuyeau, F.; Constantin, L.V.; Costescu, A.; Predoi, D. Synthesis, structure, and luminescent properties of europium-doped hydroxyapatite nanocrystalline powders. *J. Nanomater.* **2012**, *2012*, 942801. [CrossRef]

22. Predoi, D.; Iconaru, S.L.; Predoi, M.V.; Motelica-Heino, M.; Guegan, R.; Buton, N. Evaluation of antibacterial activity of zinc-doped hydroxyapatite colloids and dispersion stability using ultrasounds. *Nanomaterials* **2019**, *9*, 515. [CrossRef] [PubMed]

23. Ciobanu, C.S.; Iconaru, S.L.; Popa, C.L.; Motelica-Heino, M.; Predoi, D. Evaluation of samarium doped hydroxyapatite, ceramics for medical application: Antimicrobial activity. *J. Nanomater.* **2015**, *2015*, 849216. [CrossRef]

24. Ciobanu, C.S.; Constantin, L.V.; Predoi, D. Structural and physical properties of antibacterial Ag-doped nano-hydroxyapatite synthesized at 100 °C. *Nanoscale Res. Lett.* **2011**, *6*, 1–8. [CrossRef]

25. Rodriguez, L.; Matoušek, J. Preparation of TiO$_2$ sol-gel layers on glass. *Ceram. Silik.* **2003**, *47*, 28–31.

26. Predoi, D.; Iconaru, S.L.; Predoi, M.V. Dextran-coated zinc-doped hydroxyapatite for biomedical applications. *Polymers* **2019**, *11*, 886. [CrossRef]

27. Gwyddion. Available online: http://gwyddion.net/ (accessed on 20 January 2020).

28. Jastrzebski, W.; Sitarz, M.; Rokita, M.; Bułat, K. Infrared spectroscopy of different phosphates structures. *Spectrochim. Acta A Mol. Biomol. Spectrosc.* **2011**, *79*, 722–727. [CrossRef]

29. Iconaru, S.L.; Prodan, A.M.; Turculet, C.S.; Beuran, M.; Ghita, R.V.; Costescu, A.; Groza, A.; Chifiriuc, M.C.; Chapon, P.; Gaiaschi, S.; et al. Enamel based composite layers deposited on titanium substrate with antifungal activity. *J. Spectrosc.* **2016**, *2016*, 4361051. [CrossRef]

30. ASTM International. *ASTM E2149–13a Standard Test Method for Determining the Antimicrobial Activity of Antimicrobial Agents under Dynamic Contact Conditions*; ASTM International: West Conshohocken, PA, USA, 2013.

31. Fuchs, A.V.; Ritz, S.; Pütz, S.; Mailänder, V.; Landfester, K.; Ziener, U. Bioinspired phosphorylcholine containing polymer films with silver nanoparticles combining antifouling and antibacterial properties. *Biomater. Sci.* **2013**, *1*, 470–477. [CrossRef]

32. Predoi, D.; Iconaru, S.L.; Predoi, M.V.; Buton, N.; Motelica-Heino, M. Zinc doped hydroxyapatite thin films prepared by sol-gel spin coating procedure. *Coatings* **2019**, *9*, 156. [CrossRef]

33. ImageJ. Available online: http://imagej.nih.gov/ij (accessed on 10 January 2018).

34. Predoi, D.; Iconaru, S.L.; Predoi, M.V.; Buton, N.; Megier, C.; Motelica-Heino, M. Biocompatible layers obtained from functionalized iron oxide nanoparticles in suspension. *Coatings* **2019**, *9*, 773. [CrossRef]

35. Iconaru, S.L.; Motelica-Heino, M.; Predoi, D. Study on europium-doped hydroxyapatite nanoparticles by fourier transform infrared spectroscopy and their antimicrobial properties. *J. Spectrosc.* **2013**, *2013*, 284285. [CrossRef]

36. Ciobanu, C.S.; Iconaru, S.L.; Le Coustumer, P.; Constantin, L.V.; Predoi, D. Antibacterial activity of silver-doped hydroxyapatite nanoparticles against gram-positive and gram-negative bacteria. *Nanoscale Res. Lett.* **2012**, *7*, 324. [CrossRef] [PubMed]

37. Fowler, B.O. Infrared studies of apatites. I. Vibrational assignments for calcium, strontium, and barium hydroxyapatites utilizing isotopic substitution. *Inorg. Chem.* **1974**, *13*, 194–207. [CrossRef]

38. Kaciulis, S.; Mattogno, G.; Pandolfi, L.; Cavalli, M.; Gnappi, G.; Montenero, A. XPS study of apatite-based coatings prepared by sol-gel technique. *Appl. Surf. Sci.* **1999**, *151*, 1–5. [CrossRef]

39. Moulder, J.F.; Stickle, W.F.; Sobol, P.E.; Bomben, K.D. *Handbook of X-ray Photoelectron Spectroscopy*; Physical Electronics Inc.: Chanhassen, MN, USA, 1995.

40. Zhang, S. *Biological and Biomedical Coatings Handbook: Applications*, 1st ed.; CRC Press, Taylor & Francis Group: London, UK, 2016.

41. Massaro, C.; Baker, M.A.; Cosentino, F.; Ramires, P.A.; Klose, S.; Milella, E. Surface and biological evaluation of hydroxyapatite-based coatings on titanium deposited by different techniques. *J. Biomed. Mater. Res.* **2001**, *58*, 651–657. [CrossRef]

42. Gaggiotti, G.; Galdikas, A.; Kaciulis, S.; Mattongo, G.; Setkus, A. Surface chemistry of tin oxide based gas sensors. *J. Appl. Phys.* **1994**, *76*, 4467. [CrossRef]

43. Kawabe, T.; Shimomura, S.; Karasuda, T.; Tabata, K.; Suzuki, E.; Yamaguchi, Y. Photoemission study of dissociatively adsorbed methane on a pre-oxidized SnO_2 thin film. *Surf. Sci.* **2000**, *448*, 101–107. [CrossRef]

44. Hegde, M.S.; Ayyoob, M. O^{2-} and O^{1-} types of oxygen species on Ni and barium-dosed Ni and Cu surfaces. *Surf. Sci.* **1986**, *173*, L635–L640. [CrossRef]

45. Rao, C.N.R.; Vijayakrishnan, V.; Kulkarni, G.U.; Rajumon, M.K. A comparative study of the interaction of oxygen with clusters and single-crystal surfaces of nickel. *Appl. Surf. Sci.* **1995**, *84*, 285–289. [CrossRef]

46. Kulkarni, G.U.; Rao, C.N.R.; Roberts, M.W. Coadsorption of dioxygen and water on the Ni(110) surface: Role of O1-type species in the dissociation of water. *Langmuir* **1995**, *11*, 2572–2575. [CrossRef]

47. Mirzaee, M.; Vaezi, M.; Palizdar, Y. Synthesis and characterization of silver doped hydroxyapatite nanocomposite coatings and evaluation of their antibacterial and corrosion resistance properties in simulated body fluid. *Mater. Sci. Eng. C* **2016**, *69*, 675–684. [CrossRef] [PubMed]

48. Stoica, T.F.; Morosanu, C.; Slav, A.; Stoica, T.; Osiceanu, P.; Anastasescu, C.; Gartner, M.; Zaharescu, M. Hydroxyapatite films obtained by sol-gel and sputtering. *Thin Solid Films* **2008**, *516*, 8112–8116. [CrossRef]

49. Battistoni, C.; Casaletto, M.P.; Ingo, G.M.; Kaciulis, S.; Mattogno, G.; Pandolfi, L. Surface characterization of biocompatible hydroxyapatite coatings. *Surf. Interface Anal.* **2000**, *29*, 773–781. [CrossRef]

50. Jørgensen, B.; Christiansen, M. Samarium films on copper single crystals. *Surf. Sci.* **1991**, *251–252*, 519–523. [CrossRef]

51. Wei, L.; Yang, Y.; Xia, X.; Fan, R.; Su, T.; Shi, Y.; Yu, J.; Lia, L.; Jiang, Y. Band edge movement in dye sensitized Sm-doped TiO$_2$ solar cells: A study by variable temperature spectroelectrochemistry. *RSC Adv.* **2015**, *5*, 70512–70521. [CrossRef]

52. Iconaru, S.L.; Prodan, A.M.; Buton, N.; Predoi, D. Structural characterization and antifungal studies of Zinc-doped hydroxyapatite coatings. *Molecules* **2017**, *22*, 604. [CrossRef]

53. Iconaru, S.L.; Stanciu, G.A.; Hristu, R.; Ghita, R.V. Properties of Samarium doped hydroxyapatite thin films deposited by evaporation. *Rom. Rep. Phys.* **2017**, *69*, 508.

54. Patel, D.V.; McGhee, C.N. Contemporary in vivo confocal microscopy of the living human cornea using white light and laser scanning techniques: A major review. *Clin. Exp. Ophthalmol.* **2007**, *35*, 71–88. [CrossRef]

55. Pawley, J.B. *Handbook of Biological Confocal Microscopy*, 3rd ed.; Springer: Boston, MA, USA, 2006; pp. 20–42.

56. Bobbarala, V. *Antimicrobial Agents*; IntechOpen: London, UK, 2012.

57. Jankauskaitė, V.; Abzalbekuly, B.; Lisauskaitė, A.; Procyčevas, I.; Fataraitė, E.; Vitkauskienė, A.; Janakhmetov, U. Silicone rubber and microcrystalline cellulose composites with antimicrobial properties. *Mater. Sci.* **2014**, *20*, 42–49. [CrossRef]

58. Kramer, A.; Schwebke, I.; Kampf, G. How long do nosocomial pathogens persist on inanimate surfaces? A systematic review. *BMC Infect. Dis.* **2006**, *6*, 1–8. [CrossRef] [PubMed]

59. Predoi, D.; Iconaru, S.L.; Buton, N.; Badea, M.L.; Marutescu, L. Antimicrobial activity of new materials based on lavender and basil essential oils and hydroxyapatite. *Nanomaterials* **2018**, *8*, 291. [CrossRef] [PubMed]

60. Predoi, D.; Iconaru, S.L.; Predoi, M.V.; Groza, A.; Gaiaschi, S.; Rokosz, K.; Raaen, S.; Negrila, C.C.; Prodan, A.-M.; Costescu, A.; et al. Development of cerium-doped hydroxyapatite coatings with antimicrobial properties for biomedical applications. *Coatings* **2020**, *10*, 516. [CrossRef]

61. Morais, D.S.; Rodrigues, M.A.; Lopes, M.A.; Coelho, M.J.; Maurıcio, A.C.; Gomes, R.; Amorim, I.; Ferraz, M.P.; Santos, J.D.; Botelho, C.M. Biological evaluation of alginate-based hydrogels, with antimicrobial features by Ce(III) incorporation, as vehicles for a bone substitute. *J. Mater. Sci. Mater. Med.* **2013**, *24*, 2145–2155. [CrossRef] [PubMed]

62. Jouanny, I.; Labdi, S.; Aubert, P.; Buscema, C.; Maciejak, O.; Berger, M.-H.; Guipont, V.; Jeandin, M. Structural and mechanical properties of titanium oxide thin films for biomedical application. *Thin Solid Films* **2010**, *518*, 3212–3217. [CrossRef]

63. Dussan, A.; Bertel, S.D.; Melo, S.F.; Mesa, F. Synthesis and characterization of porous silicon as hydroxyapatite host matrix of biomedical applications. *PLoS ONE* **2017**, *2017*, e0173118. [CrossRef]

64. Xu, Y.; Hu, X.; Kundu, S.; Nag, A.; Afsarimanesh, N.; Sapra, S.; Mukhopadhyay, S.C.; Han, T. Silicon-based sensors for biomedical applications: A Review. *Sensors* **2019**, *19*, 2908. [CrossRef]

65. Ruffino, F.; Torrisi, V. Ag films deposited on Si and Ti: How the film-substrate interaction influences the nanoscale film morphology. *Superlattices Microstruct.* **2017**, *111*, 81–89. [CrossRef]

66. Barry, J.N.; Cowley, A.; McNally, P.J.; Dowling, D.P. Influence of substrate metal alloy type on the properties of hydroxyapatite coatings deposited using a novel ambient temperature deposition technique. *J. Biomed. Mater. Res. A* **2014**, *102*, 871–879. [CrossRef]

67. Ferraris, S.; Yamaguchi, S.; Barbani, N.; Cristallini, C.; Gautier di Confiengo, G.; Barberi, J.; Cazzola, M.; Miola, M.; Vernè, E.; Sprian, S. The mechanical and chemical stability of the interfaces in bioactive materials: The substrate-bioactive surface layer and hydroxyapatite bioactive surface layer interfaces. *Mater. Sci. Eng. C* **2020**, *116*, 111238. [CrossRef]

68. Zhao, S.F.; Jiang, Q.H.; Peel, S.; Wang, X.X.; He, F.M. Effects of magnesium-substituted nanohydroxyapatite coating on implant osseointegration. *Clin. Oral Implants Res.* **2013**, *24*, 34–41. [CrossRef] [PubMed]

69. Cai, Y.L.; Zhang, J.J.; Zhang, S.; Venkatraman, S.S.; Zeng, X.T.; Du, H.J.; Mondal, D. Osteoblastic cell response on fluoridated hydroxyapatite coatings: The effect of magnesium incorporation. *Biomed. Mater.* **2010**, *5*, 054114. [CrossRef] [PubMed]

70. Oliveira, A.L.; Mano, J.F.; Reis, R.L. Nature-inspired calcium phosphate coatings: Present status and novel advances in the science of mimicry. *Curr. Opin. Solid State Mater. Sci.* **2003**, *7*, 309–318. [CrossRef]